Wavelength-Controlled Photocurrent Polarity Switching in BP-MoS$_2$ Heterostructure

Himani Jawa, Abin Varghese, Sayantan Ghosh, Srilagna Sahoo, Yuefeng Yin, Nikhil V Medhekar, and Saurabh Lodha*

Layered 2D van der Waals semiconductors and their heterostructures have been shown to exhibit positive photoconductance (PPC) in many studies. A few recent reports have demonstrated negative photoconductance (NPC) as well that can enable broadband photodetection besides multi-level optoelectronic logic and memory. Controllable and reversible switching between PPC and NPC is a key requirement for these applications. This report demonstrates visible-to-near infrared wavelength-driven NPC and PPC, along with reversible switching between the two, in an air stable, high mobility, broadband black phosphorus field effect transistor covered with a few layer MoS$_2$ flake. The crossover switching wavelength can be tuned by varying the MoS$_2$ bandgap through its flake thickness and the NPC and PPC photoresponsivities can be modulated using electrostatic gating as well as laser power. Recombination-driven NPC and PPC, as supported by density functional theory calculations, allows for reversible switching. Further, gate voltage-dependent negative persistent photoconductance is well-suited for optosynaptic applications.

1. Introduction

Heterostructures based on layered van der Waals (vdW) materials have recently gained significant interest owing to the realization of a variety of optical[1–8] and electrical[9,10] phenomena. Stacking different 2D materials offers various advantages such as a wide optical detection range, enhanced photoresponse due to ease of carrier separation, clean interfaces due to the absence of dangling bonds and defects resulting from lattice mismatch. This makes them an excellent choice for photodetection applications. Generally, the device architecture and choice of 2D materials in these heterostructures have been shown to enhance the positive photoconductance[1,11–14] (PPC) for application areas such as photodetectors[15] or optical memories.[16,17]

However, some recent studies have also shown the possibility of realizing negative photoconductance[18–23] (NPC) in 2D material-based devices.

The observation of negative photoconductance along with PPC in photodetectors can enable broadband photoresponse with enhanced spectral resolution[24] due to their ability to segregate different wavelengths with distinct conductance states. Furthermore, the availability of additional states (PPC and NPC) expands the application scope of 2D materials to multi-bit logic and memory devices. However, the ability to switch reversibly and controllably between NPC and PPC is a critical and unexplored requirement for the realization of logic, memory and optical communication technologies.[18] In addition, NPC, as observed in 2D materials-based devices,[25,26] could be related to trap centers,[27] interaction with adsorbates,[28] the bolometric effect,[29] or dependent on gate bias.[20] The first three mechanisms increase carrier scattering in the device resulting in mobility degradation and negative photocurrent. Interface/adsorbate/bulk trap-related mechanisms are difficult to control since it is not trivial to engineer trap densities, distributions and time constants, whereas gate voltage-dependent NPC and PPC adds to the overall power consumption. Recently NPC has been reported in a WS$_2$/rGO hybrid structure under infrared light as a result of recombination between photogenerated electrons in WS$_2$ with holes in rGO.[19] NPC has also been reported in an ReS$_2$/hBN/MoS$_2$ heterostructure floating gate device with excellent memory properties.[18] These recent reports suggest new avenues for realizing NPC and controlled NPC-PPC switching based on heterostructures using 2D materials.

In this work, we demonstrate wavelength-driven (visible-to-near infrared) NPC and PPC, along with reversible switching between the two, in an air-stable black phosphorus (BP) FET covered with a few layer MoS$_2$ flake. BP is chosen for its high hole mobility and broad spectral response (visible as well as near infrared) and MoS$_2$ is chosen for its air-stability, optical bandgap tunability and spectral response in the visible range. The NPC is a consequence of light absorption in the MoS$_2$ flake, which results in photocarrier generation. Photogenerated holes are captured by intrinsic traps in MoS$_2$ whereas the photogenerated electrons diffuse towards the BP/MoS$_2$ interface for interlayer, or further into the BP for intralayer, recombination with holes

H. Jawa, A. Varghese, S. Ghosh, S. Sahoo, S. Lodha
Department of Electrical Engineering
IIT Bombay
Mumbai 400076, India
E-mail: slodha@ee.iitb.ac.in
A. Varghese, Y. Yin, N. V. Medhekar
Department of Materials Science and Engineering
Monash University
Clayton, Victoria 3800, Australia

The ORCID identification number(s) for the author(s) of this article can be found under https://doi.org/10.1002/adfm.202112696.

in the BP channel. Electron transport further into the BP layers is enabled by a reduction in the interface conduction band offset in thicker BP/MoS$_2$ heterostructures as inferred from density functional theory (DFT) calculations. The electron–hole recombination leads to a reduction in the net device current under illumination. As the wavelength is increased beyond the absorption edge of the MoS$_2$ flake, the phototransistor exhibits PPC solely based on the positive photoresponse of the BP flake. The critical wavelength for the crossover between NPC and PPC can be tuned through an appropriate choice of the MoS$_2$ flake thickness that determines its bandgap and absorption edge. The wavelength-driven NPC-PPC switching is reversible over multiple wavelength cycles, and the negative and positive photoresponsivities in the visible and near infrared (NIR) regimes can be tuned using electrostatic gating or laser power. Hence, a broad and tunable spectral response with distinct NPC and PPC regimes, that can be reversibly switched between using wavelength-cycling, has been realized in a BP/MoS$_2$ heterostructure phototransistor. The presence of gate voltage-dependent negative persistent photoconductance makes this device promising for optosynaptic applications as well.

2. Results and Discussion

2.1. Device Fabrication and Electrical Characterization

BP flakes were mechanically exfoliated on a 90 nm SiO$_2$/Si substrate using scotch tape. Source/drain contacts were then formed on the few layer BP flake using electron beam lithography (EBL) and metal deposition (Cr/Au ≈ 5/40 nm). An additional contact was fabricated adjacent to the source/drain contacts of the BP field effect transistor (FET). Next, MoS$_2$ flakes were mechanically exfoliated onto a polydimethylsiloxane (PDMS) stamp and large, thin flakes were transferred on to the FET to ensure complete coverage of the BP flake and the extra contact. Further, contacts were formed on the MoS$_2$ flake using EBL and metal deposition (Cr/Au ≈ 5/40 nm). Table S1, Supporting Information shows a set of 11 such devices with their respective BP and MoS$_2$ flake thicknesses. **Figure 1**a shows a schematic of the BP/MoS$_2$ phototransistor (device 1). An optical microscope image of the fabricated device is shown in Figure 1b with the phototransistor covered with an hBN flake (≈10 nm) to preclude any trapping effects from adsorbates on the electrical and optical characterization of the phototransistor. The contacts, labeled in the figure are as follows: contacts 1 and 2 sandwiched between BP and MoS$_2$ flakes for BP/MoS$_2$ phototransistor, contacts 2 and 3 being formed below the MoS$_2$ flake in order to quantitatively segregate its contribution in the phototransistor, and contacts 4 and 5 formed on top of the MoS$_2$ flake to understand its individual optical behavior. To check the crystallinity of the flakes after fabrication, Raman scans for individual materials as well as the overlap region were done. As shown in Figure 1c, Raman peaks at 384 and 405.56 cm^{-1} correspond to E$_{2g}$ (in-plane vibration) and A$_{1g}$ (out-of-plane vibration) modes for MoS$_2$ whereas peaks at 363.1, 439.7, and 467.5 cm^{-1} indicate the A$_{1g}$, B$_{2g}$, and A$_{2g}$ peaks for the BP flake. The characteristic peaks for both materials being distinctly present in the overlap region confirms the crystalline nature of the exfoliated flakes. Further, thickness of BP and MoS$_2$ flakes obtained using atomic force microscopy (AFM) are shown in Figure 1d.
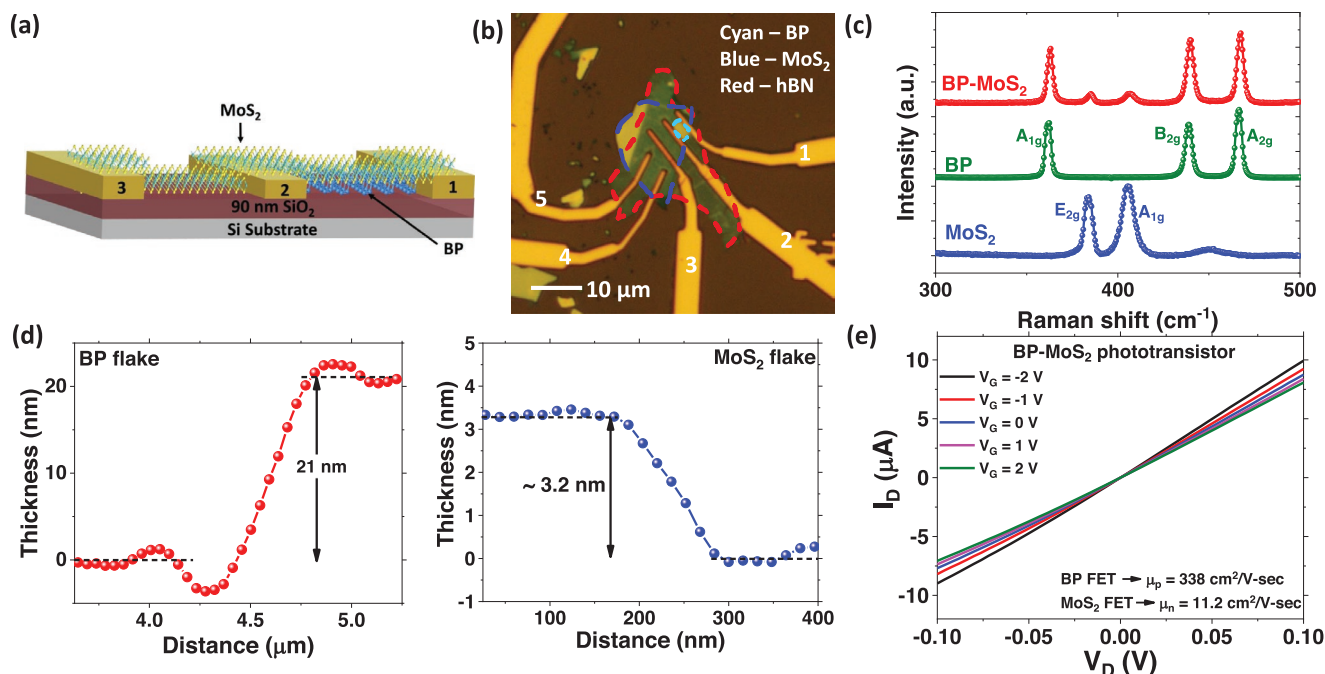

Figure 1. Device schematic, fabrication and characterization. a) Schematic of BP/MoS$_2$ phototransistor. b) Optical microscope image showing BP/MoS$_2$ phototransistor with source/drain metal contacts sandwiched between BP and MoS$_2$ layers. hBN flake on the top precludes any ambient effects. c) Raman spectra acquired for the BP/MoS$_2$ phototransistor. d) AFM scan for BP and MoS$_2$ flakes. e) Output characteristics of the phototransistor showing ohmic contacts and low gate modulation.

Individual field effect transistor performances were studied for the BP and MoS$_2$ FETs. Their transfer and output characteristics are shown in Figure S1, Supporting Information. The BP FET, with a hole mobility of 338 cm^2 V^{-1} s^{-1} (calculated at maximum transconductance) shows low gate modulation in its transfer characteristics (I_D–V_G) measured in a range of $-2 < V_G < 5$ V, shown in Figure S1a, Supporting Information, with a high positive threshold voltage (> 5 V). Similarly the extent of gate modulation of BP FETs measured over a fixed gate voltage range corresponding to the devices listed in Table S1, Supporting Information, varied depending on the thickness-dependent threshold voltage of the BP flake, as shown in Figure S2, Supporting Information. The trend in threshold voltage, and hence the gate modulation over a fixed gate voltage range, with thickness of BP flakes is consistent with previous reports on MoS$_2$[30] and MoTe$_2$[31] FETs. On the other hand, the MoS$_2$ FET, measured between contacts 4 and 5 of device 1, shows good gate tunability of I_D (shown in Figure S1c, Supporting Information) with an electron mobility of ≈11 cm^2 V^{-1} s^{-1}. The output characteristics of the MoS$_2$ FET with contacts below (contacts 2 and 3) and above the flake (contacts 4 and 5) highlight their ohmic behavior with the currents being slightly higher for contacts 4 and 5 made above the flake, as shown in Figure S1b,d, Supporting Information. The output (I_D–V_D) characteristics of the phototransistor, as shown in Figure 1e, indicate a major contribution to the current from the BP flake (≈µAs) as compared to a few nAs from the MoS$_2$ flake with low gate modulation. Additionally, covering the BP

flake with the MoS$_2$ flake results in stable device characteristics of the BP/MoS$_2$ phototransistor, as shown in Figure S3, Supporting Information.

2.2. Optoelectronic Characterization of the BP/MoS$_2$ Phototransistor

Photoresponse of the BP/MoS$_2$ heterostructure was obtained under 690–900 nm laser illumination. The light was incident on the phototransistor for 30 s and then turned off. The photoresponsivity (R) was calculated using the equation: $R = I_{ph}/P_{in}$, where $I_{ph} = I_{light} - I_{dark}$ with I_{light} and I_{dark} being the currents with and without illumination and P_{in} is the incident optical power. As shown in **Figure 2**a, responsivity is negative for wavelengths (λ) upto 720 nm and positive beyond 750 nm for gate (V_G) and drain (V_D) voltages of 0 and 0.1 V respectively. The negative R can be explained from the band alignment of the BP and MoS$_2$ flakes in the transverse direction (along gate-SiO$_2$-BP-MoS$_2$). Under equilibrium, BP/MoS$_2$ forms a type-II heterostructure with a band alignment as shown in Figure 2c(i). This is also seen in our first-principles based DFT calculations of the bandstructure of 2L BP/2L MoS$_2$ heterostructure, as shown in Figure S7, Supporting Information. Both BP and MoS$_2$ absorb visible light ($\lambda < 750$ nm) illuminated on the overlap region, with MoS$_2$ absorbing more than BP, thereby leading to generation of electron–hole pairs. The photogenerated holes in MoS$_2$ get captured by the shallow intrinsic
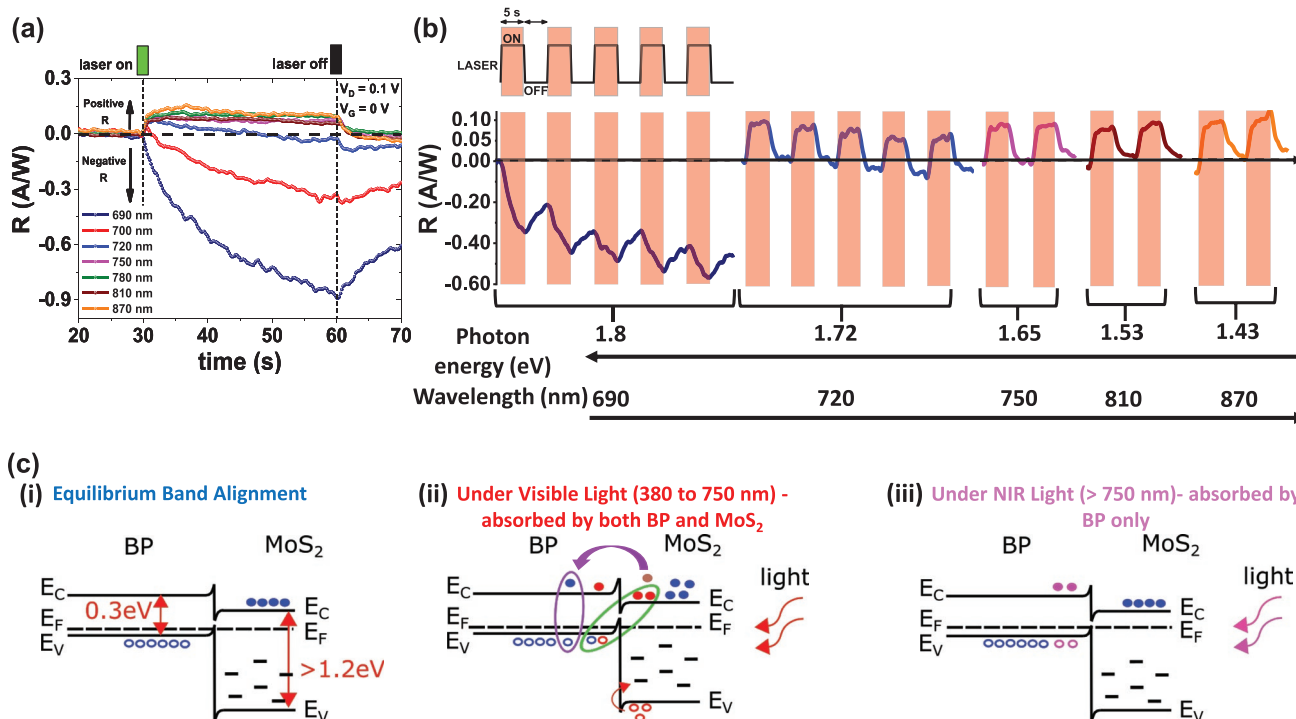

Figure 2. Wavelength-dependent photoconductance and related band diagrams. a) Responsivity versus time for the BP/MoS$_2$ phototransistor showing negative responsivity for $\lambda < 750$ nm and positive responsivity for $\lambda > 750$ nm at $V_G = 0$ V and $V_D = 0.1$ V. b) Photoswitching with on and off time being 5 s at $V_G = 0$ V and $V_D = 0.1$ V for different wavelengths. c) BP-MoS$_2$ energy band alignment at $V_G = 0$ V for i) equilibrium conditions, ii) under visible light, where both BP and MoS$_2$ absorb light resulting in recombination and hence, negative photocurrent, and iii) for NIR illumination, which is absorbed only by the BP flake and hence, positive photocurrent is observed.

**ADVANCED
SCIENCE NEWS**

www.advancedsciencenews.com

**ADVANCED
FUNCTIONAL
MATERIALS**

www.afm-journal.de

traps distributed near its valence band[32] giving rise to excess electron concentration. These excess electrons diffuse toward BP/MoS$_2$ interface due to the concentration gradient set up by a lower concentration in BP leading to interlayer recombination of the electrons directly with the high hole concentration of BP. Further, a comparison of bandstructure plots (Figure S7, Supporting Information) of thick (2L BP/2L MoS$_2$) and thin (1L BP/1L MoS$_2$) heterostructures shows a reduction in the interface conduction band offset in the thicker structure which also makes the transport of electrons from the conduction band of MoS$_2$ to the conduction band of BP feasible. This could enable intralayer recombination of electron–hole pairs in BP, as shown in Figure 2c(ii). These mechanisms result in a reduction in free hole concentration in BP giving rise to a negative photocurrent or responsivity (as seen in Figure 2a), since BP is the main photoconducting layer in this BP-MoS$_2$ stack. As the wavelength is increased beyond 750 nm, a positive I_{ph} is observed which can be attributed to i) negligible optical response from the thin MoS$_2$ flake limited by its bandgap and ii) photogenerated carriers in the smaller bandgap (0.3 eV) BP flake. Other mechanisms for NPC can be excluded based on the following reasons. First, the bolometric effect can be excluded based on the high thermal conductivity of the Si/SiO$_2$ substrate as compared to flexible substrates[29] and the absence of NPC in NIR regime[33]; second, trapping at the channel-dielectric interface can be ruled out due to the absence of gate-dependent NPC-to-PPC transition (as shown in Figure S8, Supporting Information),[20,21] and finally, the effect of adsorbates on NPC can be excluded as the BP/MoS$_2$ phototransistor is covered with an hBN flake. The optical response of the MoS$_2$ FET (contacts 4 and 5) to 4 incident wavelengths (690, 720, 750, and 780 nm) is shown in Figure S9a, Supporting Information. MoS$_2$ does not respond to illumination beyond 720 nm due to its bandgap and therefore, the crossover wavelength λ_t, defined as the wavelength at which the I_{ph} transitions from negative to positive values, is limited by the bandgap of MoS$_2$. Figure 2b and Figure S10a, Supporting Information show the transition from negative to positive responsivity and photocurrent when the phototransistor was illuminated under different wavelengths with the laser being switched on and off every 5 s for each λ.

2.2.1. Gate Voltage and Laser Power Dependent Photocurrent Modulation

The recombination occurring at the BP/MoS$_2$ interface under visible light, as discussed above, depends on i) the electron concentration of MoS$_2$ (n_M) and ii) hole concentration of BP (p_{BP}). These carrier concentrations are modulated by the applied gate bias electrostatically and optically and light intensity respectively. Also, the hole concentration in BP is affected by the trapping and detrapping at the BP/SiO$_2$ interface which varies with applied gate bias.[34] This results in a dual effect of V_G on the carrier concentrations and hence, on the carrier recombination. Under illumination for varying V_G, the I_{ph} (dependent on carrier recombination) will be maximum where the effective electron and holes concentrations in MoS$_2$ and BP respectively will be nearly equal (as shown in Figure S11, Supporting Information). The I_{ph} will gradually reduce with V_G on both sides of the

maximum point due to reduction in either holes or electrons at positive and negative V_G respectively, since the recombination is limited by the minority carrier concentration (I_{ph} vs V_G at P_{in1} in Figure S11b, Supporting Information).

Figure 3a shows the variation in photocurrent with gate voltage for varying incident power of 690 nm illumination. The photocurrent magnitude shows a slight increase at lower laser powers, nearly constant trend at intermediate powers (e.g., at 0.187 µW, similar to the theoretical expectation illustrated in Figure S11b, Supporting Information) and a more pronounced change (decrease) in its value at higher optical powers. At lower optical power, most of the electron–hole pair generation takes place in MoS$_2$. Given the trapping of photogenerated holes in MoS$_2$ and a high hole concentration in BP, the recombination is limited by the MoS$_2$ electron concentration ($n_M < p_{BP}$). The electron concentration in MoS$_2$ increases with increase in gate voltage (as the device transitions from subthreshold to ON state, as shown in Figure S1c, Supporting Information). Hence, a slightly higher recombination at positive V_G leads to slightly higher I_{ph} as shown by the band diagram for point 1 in Figure 3b. At lower optical powers, we observe only the left (increasing) I_{ph} branch of the theoretically predicted curve at P_{in1} in Figure S11b, Supporting Information. As the optical intensity is increased, n_M increases due to an increase in the photogenerated carriers in MoS$_2$. This leads to recombination being limited by p_{BP}, which gets affected by the trapping and detrapping of holes at the BP/SiO$_2$ interface.[34] As V_G is reduced from positive to negative values, the traps at the BP/SiO$_2$ interface above the Fermi level (E_F) of BP get filled with holes, going from neutral to positively charged. This results in the reduction of free hole carrier concentration in BP as well as of the effective negative gate bias, similar to the left-shift in the I_{ph} curve at higher optical power P_{in2} of Figure S11b, Supporting Information. In order to compensate for this reduction in hole concentration, a more negative V_G is required and hence, maximum photocurrent is shifted toward negative V_G, as shown at point 2 in Figure 3b. In the case of higher optical powers, we observe only the right (decreasing) branch of the I_{ph} curve at P_{in2} in Figure S11b, Supporting Information.

When the phototransistor is illuminated with 780 nm laser (NIR), a positive photocurrent is observed, as shown in Figures S10b,c, Supporting Information for varying optical power and gate voltage respectively. This positive I_{ph} increases as the input incident power increases due to an increase in the photogenerated carrier concentrations in the BP flake, as shown in Figure S10b, Supporting Information. Higher variability in the photocurrent at lower laser powers can be attributed to the higher percentage variability for lower laser powers at 780 nm illumination in our setup. The photocurrent also increases as the gate voltage is increased from negative to positive values. This can be explained by increased concentration of photogenerated free carriers at positive V_G as compared to negative V_G with the maximum photocurrent occurring at maximum transconductance value.[35] This is due to dominant photogating effect at the maximum transconductance operating point. Since the BP FET is in the accumulation region for the given V_G range, the I_{ph} increases with increase in V_G.
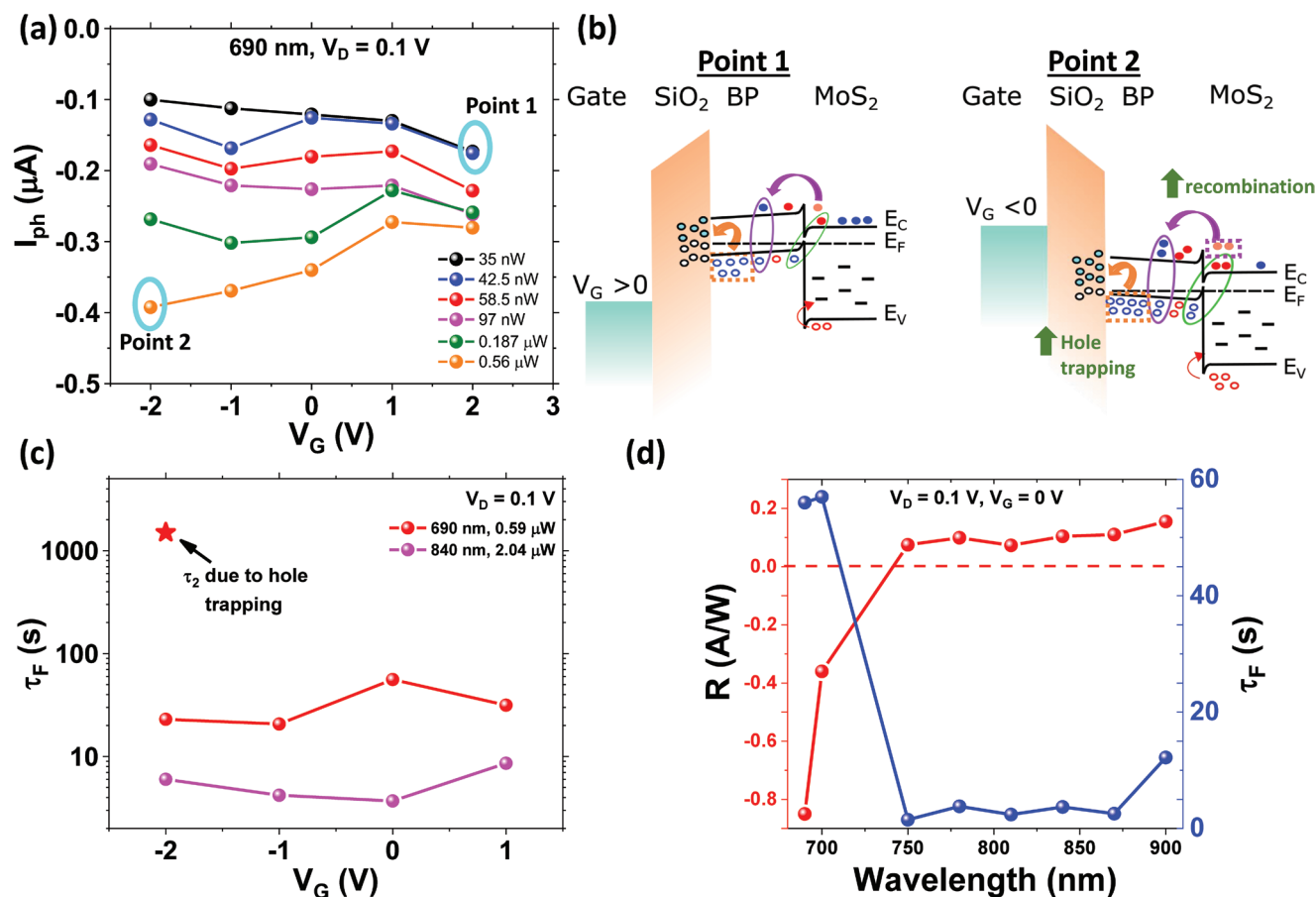
Figure 3. Gate voltage, laser power and wavelength dependence of temporal response and photocurrent. a) Variation of photocurrent as a function of gate voltage under 690 nm illumination. b) Energy band diagrams at points 1 and 2 of figure (a). c) Fall time (τ_F) vs V_G for 690 and 840 nm illumination indicates faster operation under NIR. d) Responsivity (R) and τ_F as a function of wavelength. Negative responsivity and higher fall times correspond to the optical sensing of MoS$_2$ in the phototransistor.

2.2.2. Temporal Photoresponse

Next, temporal measurements were carried out in order to understand the variation in the speed of the device for negative and positive photocurrent regimes. As shown in Figure 3c, the fall time (τ_F) remains nearly constant over gate voltage for both 690 (visible) and 840 nm (NIR) illumination. However, we observe that i) τ_F is lower in the positive I_{ph} regime, that is, under 840 nm illumination compared to 690 nm and (ii) there is a second time constant at $V_G = -2$ V ($\approx 1.5 \times 10^3$ s) which is likely due to hole trapping in the MoS$_2$ flake and at the BP/SiO$_2$ interface (discussed later in this paper). Under 690 nm illumination, free carriers in both flakes (p_{BP} and n_M) are responsible for photoconduction and negative I_{ph}. The slow response of the MoS$_2$ flake (as can be observed from the slow recovery of the MoS$_2$ FET after the laser is switched off, shown in Figure S9a, Supporting Information) due to long detrapping time of the photogenerated holes results in increased lifetime of the photogenerated electrons thereby leading to a large τ_F.[36] However, under 840 nm illumination, the positive I_{ph} arises only from the photogenerated carriers of BP thereby resulting in relatively faster optical operation or lower fall time. This can also be observed in Figure 2b where the photocurrent I_{ph}

(or photoresponsivity, R) increases in magnitude with each optical cycle under visible light as it is limited by the time constant of the carriers in the MoS$_2$ flake, however a steady on and off cycles are observed for NIR illumination due to fast hole detrapping time constant in the BP flake. Figure 3d shows variation in τ_F and R with wavelength. For $\lambda < 750$ nm, τ_F is higher (≈ 55 s) due to MoS$_2$-limited dark current recovery. For λ beyond 750 nm, lower fall times are observed due to higher mobility in the BP flake and faster detrapping time for trapped photocarriers from shallow traps in BP bulk.[35] The fall time varied across several phototransistors under 840 nm illumination with varying thickness of the BP flake.[37] Figure S12a, Supporting Information shows the normalized photocurrent with time for four additional devices along with device 1 (listed in Table S1, Supporting Information) with fall time varying from 0.6 to 2 s. Additionally, the phototransistor performance R verses τ_F under 840 nm illumination has been compared with other reported BP photodetectors in Figure S12b, Supporting Information.

2.3. MoS$_2$ Thickness Dependent Negative Photocurrent

The negative photocurrent depends on the free carrier concentrations of BP and MoS$_2$ flakes that can be modulated in
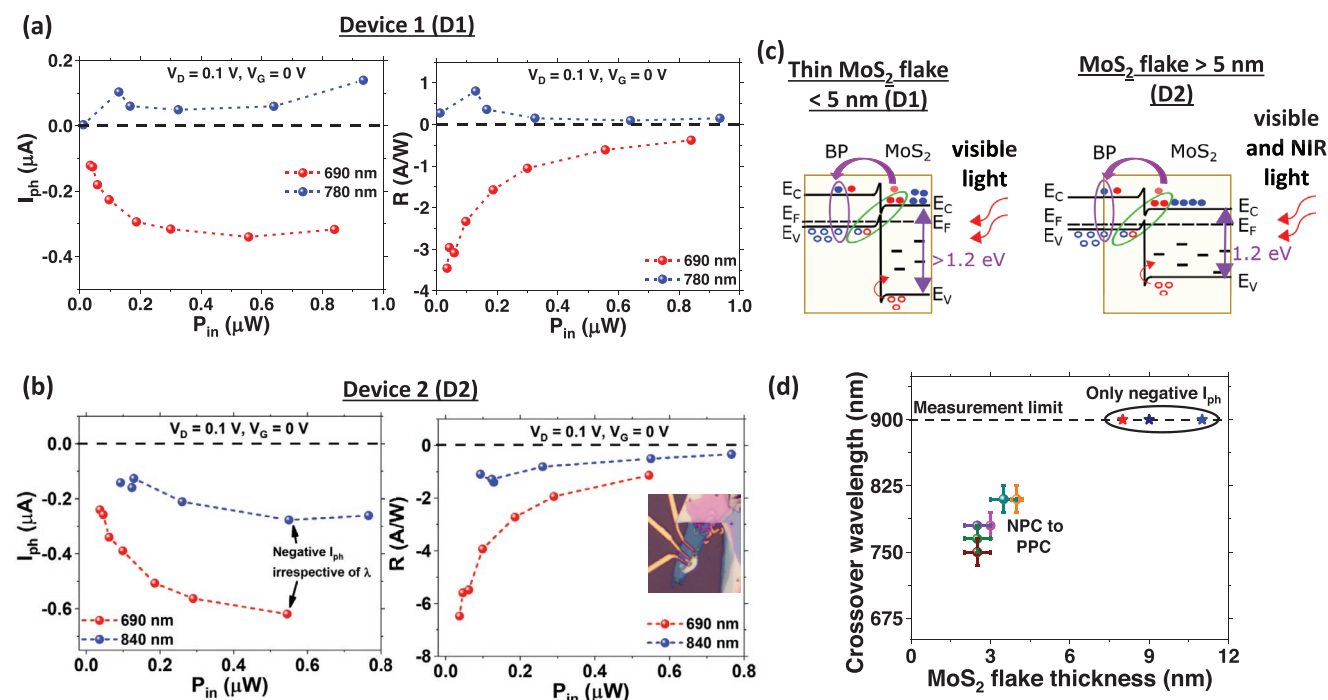
ADVANCED
SCIENCE NEWS
www.advancedsciencenews.com

ADVANCED
FUNCTIONAL
MATERIALS
www.afm-journal.de

Figure 4. MoS$_2$ thickness dependent NPC and PPC crossover wavelength. Photocurrent and responsivity as a function of input laser power for a) device 1 (MoS$_2$ thickness of ≈3 nm) and b) device 2 (MoS$_2$ thickness of 11 nm) under 690 and 840 nm illumination. Negative photocurrent in visible and NIR corroborates absorption of light by both MoS$_2$ and BP flakes. c) Band alignment in BP and MoS$_2$ with varying thickness of MoS$_2$ flake. d) MoS$_2$ thickness versus crossover wavelength, λ_t (wavelength at which the photocurrent transitions from negative to positive values).

magnitude (photoresponsivity) and spectral range by the gate voltage and the optical absorption range of the MoS$_2$ flake respectively. Given that light absorption by the MoS$_2$ flake results in generation of photocarriers that diffuse toward BP resulting in recombination and hence, negative I_{ph}, the optical spectral response of MoS$_2$ determines the crossover wavelength from NPC to PPC for the phototransistor. The spectral response of MoS$_2$ is limited by its bandgap which varies with the thickness of the flake and therefore, the crossover wavelength increases for the first few nanometers of the MoS$_2$ flake as the bandgap decreases with increasing thickness, till the bandgap becomes constant (≈1.2 eV) for a few layer MoS$_2$ flake. **Figure 4**a–c shows the optical response and corresponding band diagrams for two phototransistors with ≈3 nm and 11 nm thick MoS$_2$ flakes. Device 1 (flake thickness ≈3 nm) shows negative (positive) I_{ph} and R for 690 nm (780 nm) as its λ_t is approximately 750 nm (≈1.65 eV) which is close to the bandgap of the MoS$_2$ flake. On the other hand, the 11 nm thick MoS$_2$ flake in device 2 has a bandgap of ≈1.2 eV. Hence, it exhibits a negative optical response to both 690 and 840 nm illumination since its λ_t is greater than 1000 nm (which is difficult to demonstrate given the limitation of our measurement setup). As the flake thickness of MoS$_2$ increases further, the diffusion of electrons from the top surface (high optical absorption region) of the MoS$_2$ flake towards BP becomes less favorable. This leads to negligible recombination resulting in a direct flow of electrons from conduction band of MoS$_2$ to the contacts. This leads to a positive I_{ph} for visible and NIR illumination, as shown in Figure S13, Supporting Information (device 3). It should be noted that a few layer BP flake is selected for these phototransistors with a reasonable I_{on}/I_{off}

and a fixed bandgap of ≈0.3 eV. Similar PPC behavior was also observed in devices with thicker BP flakes over the entire wavelength range of 690 to 900 nm, irrespective of the thickness of the MoS$_2$ flake. Optical characteristics of a phototransistor with MoS$_2$ and BP flake thicknesses of 8 and 70 nm respectively are shown in Figure S14, Supporting Information. Table S4, Supporting Information consolidates the flake thickness dependent photoresponse of the BP/MoS$_2$ phototransistor. Figure 4d shows the variation of crossover wavelength with MoS$_2$ thickness for multiple devices indicating that as the MoS$_2$ flake thickness increases, λ_t increases till it saturates for few layer flakes.

2.4. Applications

The BP/MoS$_2$ device architecture gives the advantage of switching the photocurrent from negative to positive values within a time scale of a few seconds as the wavelength switches from 700 to 750 nm, as shown in **Figure 5**a. Photocurrent switching characteristics of two additional devices are shown in Figure S15, Supporting Information. This transition can be used in a wavelength-dependent multi-bit coding scheme as it helps in differentiating change in current due to different wavelengths of light thereby increasing the accuracy of light recognition. Further, this device also demonstrates negative persistent photoconductance, where the photocurrent reaches a maximum negative value under illumination and when the light is withdrawn, it holds on to a negative current value (lower than the maximum but not the same as the dark current) for a long period of time. Figure 5b shows negative persistent
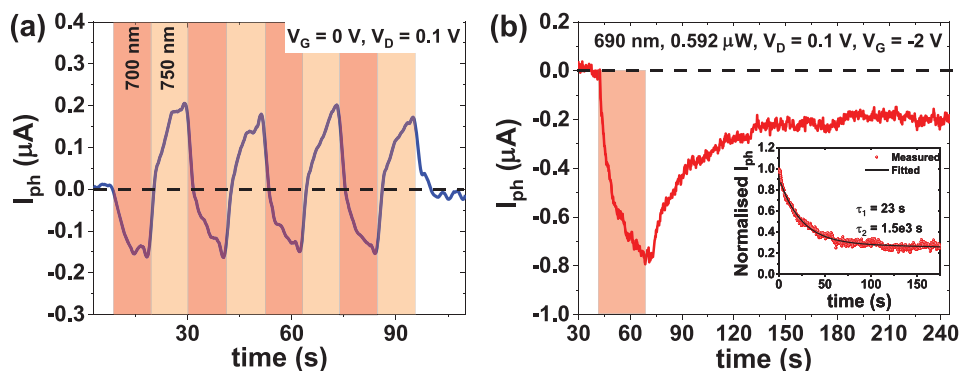
Figure 5. Wavelength-based photoswitching and negative persistent photoconductance. a) Wavelength-based photocurrent switching at $V_G = 0$ V and $V_D = 0.1$ V. b) Negative persistent photoconductance at $V_G = -2$ V and $V_D = 0.1$ V with the inset showing a double exponential-based fitting of the normalized photocurrent.

photoconductance of device 1 for $V_G = -2$ V with the normalized photocurrent Y (shown in Figure 5b inset) following a double exponential function: $Y = A_1 \exp(-t/\tau_1) + A_2\exp(-t/\tau_2)$.[38] Here t is time, A_1 and A_2 are constants and τ_1 and τ_2 are fast and slow decay time constants respectively. The faster time constant, $\tau_1 = 23$ s symbolizes rapid relaxation of the device's photocurrent in response to light withdrawal, whereas the slower time constant $\tau_2 = 1.5 \times 10^3$ s arises from hole trapping in MoS_2 or at the BP/SiO_2 interface on visible light illumination which results in slower decay in current. Specifically at negative gate voltage, the hole trapping at the BP/SiO_2 interface (shown in Figure 3b Point 2) is more as compared to positive gate voltage (shown in Figure 3b Point 1), resulting in a reduced free hole concentration in the BP channel. The slow detrapping of these interface traps prevent the current from returning to its dark value as soon as the light is withdrawn resulting in retention of a negative photocurrent at negative gate voltage. This behavior

is similar to the long term potentiation observed in synaptic devices. Given that the negative persistent photoconductivity in the BP/MoS_2 phototransistor is a consequence of carrier recombination at the BP/MoS_2 heterointerface and hole trapping at the $BP-SiO_2$ interface, as shown in Figure 3b Point 2, the negative persistent photoconductance states can likely be tuned by gate voltage as well as wavelength ($\lambda < \lambda_t$). Similar behavior for another device (device 6) along with all its other optical measurements is shown in Figure S16, Supporting Information.

2.5. Conclusions

This work demonstrates wavelength-dependent photoconductance polarity and reversible NPC-PPC switching in a BP/MoS_2 phototransistor. **Table 1** compares the key optical characteristics of various architectures and devices using 2D materials that demonstrate negative photoconductance along

Table 1. Comparison of this work with previous studies demonstrating negative photoconductance.

Ref.	Material	Spectral response [nm]	NPC and PPC	NPC ↔ PPC modulator	Mechanism	NPC-to-PPC switching		Application
						Modulator	Reversible	
[29]	BP	830	Only NPC	NIR	Bolometric effect			
[39]	MoS_2	NIR	Only NPC	Monolayer MoS_2	Trion Formation			
[33]	MoS_2	454, 519, 625, 980 and 1550	Both	NIR	Bolometric effect			
[18]	ReS_2/hBN /MoS_2	520, 637, 830, and 1310	Both	V_G and λ	Charge trapping			Photoelectronic memory
[19]	WS_2/ RGO	808	Only NPC	NIR	Recombination			
[20]	BP/ $SnS_{0.5}Se_{1.5}$	365 894.6	Both	V_G	Charge trapping			
[21]	Gr/BP	655, 785 980	Both	V_G	Electron trapping			
[22]	$MoSe_2$/Gr	450–1000	Both	V_G	Charge transfer			
[23]	Gr/MoS_2	635	Both	V_G	Charge transfer			
[40]	$MoTe_2$/Gr	975	Both	laser power	Charge transfer	laser power	Yes	
This work	BP/MoS_2	690–900	Both	$\lambda \approx MoS_2$ bandgap	Recombination	λ	Yes	Photoelectronic memory

with the BP/MoS$_2$ phototransistor reported in this work. The NPC is a result of recombination between photogenerated electrons in MoS$_2$ with holes in the BP flake. The NPC-to-PPC crossover wavelength is tunable with the thickness of the MoS$_2$ flake. MoS$_2$ thickness modulates its bandgap and optical absorption range thereby resulting in NPC (PPC) for wavelengths within (beyond) the absorption range. The device offers dual fold application: first, different photoelectric response to different wavelengths, owing to the presence of both NPC and PPC in the same device, expands its application prospects to broadband photoelectric sensing and second, the presence of negative persistent photoconductance at negative gate voltage offers a promising avenue for opto-controlled synaptic applications.

3. Experimental Section

The BP transistors were fabricated using a degenerately doped p-type Si substrate with 90 nm thermally grown SiO$_2$. BP flakes were mechanically exfoliated using Scotch Tape and transferred onto the substrate. The flakes were then identified using an optical microscope and source/drain contacts (along with an additional adjacent contact) were patterned by electron beam lithography (Raith 150-Two) using poly(methyl methacrylate) resist. Source/drain metal (Cr/Au –5/40 nm) was deposited using sputtering followed by lift-off. Further, MoS$_2$ flakes were mechanically exfoliated from the molybdenite crystal using PDMS and were transferred on the fabricated BP FET using a pick-and-transfer process using a micromanipulator setup. The contacts on MoS$_2$ were fabricated using e-beam lithography and metal deposition. The final device image was taken using a Olympus BX-63 microscope and the SEM imaging was done using Raith 150-Two. ULVAC-PHI/PHI5000 Versa ProbeII focus X-ray photoelectron spectrometer was used for XPS measurements and Horiba HR 800 Raman spectroscopy system with a 532 nm laser was used for Raman imaging. Before optical characterization, the device was placed on a PCB with large gold contact pads. The device contact pads were wire bonded using gold wire to the large PCB contact pads. The optoelectronic measurements were done in ambient conditions under a BX-63 Olympus microscope using a Keysight B1500A semiconductor device analyzer using an NKT laser with a wavelength range of 690 to 900 nm. Switching of laser power was done using input of square pulses of 10 V peak-to-peak to the laser power controller unit from an Agilent 33220A function generator. The laser was incident on the device through the objective lens of the BX-63 Olympus microscope.

Supporting Information

Supporting Information is available from the Wiley Online Library or from the author.

Conflict of Interest

The authors declare no conflict of interest.

Data Availability Statement

The data that support the findings of this study are available from the corresponding author upon reasonable request.

[1] A. Varghese, D. Saha, K. Thakar, V. Jindal, S. Ghosh, N. V. Medhekar, S. Ghosh, S. Lodha, *Nano Lett.* **2020**, *20*, 1707.

[2] Z. Yang, L. Liao, F. Gong, F. Wang, Z. Wang, X. Liu, X. Xiao, W. Hu, J. He, X. Duan, *Nano Energy* **2018**, *49*, 103.

[3] Y. Deng, Z. Luo, N. J. Conrad, H. Liu, Y. Gong, S. Najmaei, P. M. Ajayan, J. Lou, X. Xu, P. D. Ye, *ACS Nano* **2014**, *8*, 8292.

[4] C.-H. Lee, G.-H. Lee, A. M. Van Der Zande, W. Chen, Y. Li, M. Han, X. Cui, G. Arefe, C. Nuckolls, T. F. Heinz, J. Guo, J Hone, P. Kim, *Nat. Nanotechnol.* **2014**, *9*, 676.

[5] R. Cheng, D. Li, H. Zhou, C. Wang, A. Yin, S. Jiang, Y. Liu, Y. Chen, Y. Huang, X. Duan, *Nano Lett.* **2014**, *14*, 5590.

[6] Y. Chen, X. Wang, G. Wu, Z. Wang, H. Fang, T. Lin, S. Sun, H. Shen, W. Hu, J. Wang, J. Sun, X. Meng, J. Chu, *Small* **2018**, *14*, 1703293.

[7] S.-H. Jo, H. W. Lee, J. Shim, K. Heo, M. Kim, Y. J. Song, J.-H. Park, *Adv. Sci.* **2018**, *5*, 1700423.

[8] D. Saha, A. Varghese, S. Lodha, *ACS Appl. Nano Mater.* **2019**, *3*, 820.

[9] A. K. Geim, I. V. Grigorieva, *Nature* **2013**, *499*, 419.

[10] K. Novoselov, O. A. Mishchenko, O. A. Carvalho, A. C. Neto, *Science* **2016**, *353*, 6298.

[11] K. Murali, N. Abraham, S. Das, S. Kallatt, K. Majumdar, *ACS Appl. Mater. Interfaces* **2019**, *11*, 30010.

[12] G. H. Shin, C. Park, K. J. Lee, H. J. Jin, S.-Y. Choi, *Nano Lett.* **2020**, *20*, 5741.

[13] K. Thakar, B. Mukherjee, S. Grover, N. Kaushik, M. Deshmukh, S. Lodha, *ACS Appl. Mater. Interfaces* **2018**, *10*, 36512.

[14] S. Ghosh, A. Varghese, K. Thakar, S. Dhara, S. Lodha, *Nat. Commun.* **2021**, *12*, 3336.

[15] Q. Qiu, Z. Huang, *Adv. Mater.* **2021**, *33*, 2008126.

[16] Q. Wang, Y. Wen, K. Cai, R. Cheng, L. Yin, Y. Zhang, J. Li, Z. Wang, F. Wang, F. M. Wang, T. Ahmed, S. Jiang, H. Yang, J. He, *Sci. Adv.* **2018**, *4*, eaap7916.

[17] Y. Sun, Y. Ding, D. Xie, M. Sun, J. Xu, P. Yang, Y. Zhang, T. Ren, *2D Mater.* **2021**, *8*, 025021.

[18] Y. Wang, E. Liu, A. Gao, T. Cao, M. Long, C. Pan, L. Zhang, J. Zeng, C. Wang, W. Hu, S.-J. Liang, F. Miao, *ACS Nano* **2018**, *12*, 9513.

[19] S. Ratha, A. J. Simbeck, D. J. Late, S. K. Nayak, C. S. Rout, *Appl. Phys. Lett.* **2014**, *105*, 243502.

[20] X. Luo, B. Wang, W. Lv, Y. Wang, W. Lv, Z. Wei, Y. Lu, Z. Liu, Z. Lu, R. Xiong, Z. Zeng, *ACS Appl. Nano Mater.* **2019**, *2*, 3548.

[21] J. Xu, Y. J. Song, J.-H. Park, S. Lee, *Solid-State Electron.* **2018**, *144*, 86.

[22] B. Liu, C. You, C. Zhao, G. Shen, Y. Liu, Y. Li, H. Yan, Y. Zhang, *Chin. Opt. Lett.* **2019**, *17*, 020002.

[23] K. Roy, M. Padmanabhan, S. Goswami, T. P. Sai, G. Ramalingam, S. Raghavan, A. Ghosh, *Nat. Nanotechnol.* **2013**, *8*, 826.

[24] H. Jin, Y. Chen, L. Zhang, R. Wan, Z. Zou, H. Li, Y. Gao, *Nanotechnology* **2020**, *32*, 085202.

[25] B. Cui, Y. Xing, J. Han, W. Lv, W. Lv, T. Lei, Y. Zhang, H. Ma, Z. Zeng, B. Zhang, *Chin. Phys. B* **2021**, *30*, 028507.

[26] B. H. Kim, S. H. Kwon, H. H. Gu, Y. J. Yoon, *Phys. E* **2019**, *106*, 45.

[27] X. Xiao, J. Li, J. Wu, D. Lu, C. Tang, *Appl. Phys. A* **2019**, *125*, 765.

[28] C. Biswas, F. Güneş, D. D. Loc, S. C. Lim, M. S. Jeong, D. Pribat, Y. H. Lee, *Nano Lett.* **2011**, *11*, 4682.

[29] J. Miao, B. Song, Q. Li, L. Cai, S. Zhang, W. Hu, L. Dong, C. Wang, *ACS Nano* **2017**, *11*, 6048.

[30] J. Park, D. Das, M. Ahn, S. Park, J. Hur, S. Jeon, *Nano Convergence* **2019**, *6*, 32.

[31] M. J. Mleczko, A. C. Yu, C. M. Smyth, V. Chen, Y. C. Shin, S. Chatterjee, Y.-C. Tsai, Y. Nishi, R. M. Wallace, E. Pop, *Nano Lett.* **2019**, *19*, 6352.

[32] D. Kufer, G. Konstantatos, *Nano Lett.* **2015**, *15*, 7307.

[33] J.-Y. Wu, Y. T. Chun, S. Li, T. Zhang, J. Wang, P. K. Shrestha, D. Chu, *Adv. Mater.* **2018**, *30*, 1705880.

[34] N. Goyal, S. Mahapatra, S. Lodha, *IEEE Trans. Electron Devices* **2019**, *66*, 4572.

[35] Q. Guo, A. Pospischil, M. Bhuiyan, H. Jiang, H. Tian, D. Farmer, B. Deng, C. Li, S.-J. Han, H. Wang, Q. Xia, T.-P. Ma, T. Mueller, F. Xia, *Nano Lett.* **2016**, *16*, 4648.

[36] Q. Zhao, W. Wang, F. Carrascoso-Plana, W. Jie, T. Wang, A. Castellanos-Gomez, R. Frisenda, *Mater. Horiz.* **2020**, *7*, 252.

[37] C. Hou, C. Yang, L. Li, B. Li, Q. Zhang, Y. Li, Q. Yue, Y. Wang, Z. Yang, L. Dong, *Sensors* **2018**, *18*, 1668.

[38] M. M. Islam, D. Dev, A. Krishnaprasad, L. Tetard, T. Roy, *Sci. Rep.* **2020**, *10*, 21870.

[39] C. Lui, A. Frenzel, D. Pilon, Y.-H. Lee, X. Ling, G. Akselrod, J. Kong, N. Gedik, *Phys. Rev. Lett.* **2014**, *113*, 166801.

[40] H. J. Kim, K. J. Lee, J. Park, G. H. Shin, H. Park, K. Yu, S.-Y. Choi, *ACS Appl. Mater. Interfaces* **2020**, *12*, 38563.